Validation of the -Re Transition Model for Airfoils Operating in the Very Low Reynolds Number Regime

Flow, Turbulence and Combustion
https://doi.org/10.1007/s10494-022-00331-z

Validation of the γ-Re $_\theta$ Transition Model for Airfoils Operating in the Very Low Reynolds Number Regime

Manuel Carreño Ruiz[1] · **Domenic D'Ambrosio**[1]

Received: 4 February 2022 / Accepted: 13 May 2022

Abstract
Micro Aerial Vehicles (MAVs) are state of the art in the aerospace industry and are involved in many operations. The reduced dimensions of these vehicles generate very low Reynolds number conditions in which separation-induced transition typically occurs. The extremely large computational cost of scale resolving simulations, which are capable of capturing laminar to turbulent transition, is prohibitive for most engineering and design applications. Therefore, it becomes very interesting to couple transition models with conventional Reynolds Averaged Navier–Stokes (RANS) simulations to allow the prediction of transition to turbulence at a reduced computational cost. This paper performs an investigation of the application of the γ-Re $_\theta$ transition model analysing different empirical correlations available in literature and studying the influence of the relevant model parameters using the commercial Computational Fluid Dynamics (CFD) code STAR-CCM+. The flow around the Eppler 387, Selig/Donovan 7003 and Ishii airfoils has been studied for different Reynolds numbers and angles of attack comparing the drag and lift forces and separation bubble characteristics with experimental and numerical results reported in literature.

Keywords CFD · Very low Reynolds number · Transition modelling · Separation bubbles

1 Introduction

Propellers and rotors of micro aerial vehicles typically operate at Reynolds numbers ranging between 10^4 and 10^5, a regime dominated by the presence of a laminar separation bubble that arises from the transition to turbulence and subsequent reattachment of the boundary layer. For this reason, numerical simulations using RANS approaches must couple a transition model to the adopted turbulence model. In this paper, we analyze the behavior of

Domenic D'Ambrosio have contributed equally to this work.

✉ Manuel Carreño Ruiz
manuel.carreno@polito.it

Domenic D'Ambrosio
domenic.dambrosio@polito.it

[1] Department of Mechanical and Aerospace Engineering, Politecnico di Torino, Corso Duca degli Abruzzi 24, 10124 Torino, Italy

Published online: 15 June 2022

the γ-Re $_\theta$ transition model (Menter et al. 2006; Langtry 2006) when coupled with the SST k-ω model developed by Menter (1994), to verify its capability to adequately capture laminar separation bubbles (LSB), which usually significantly degrade airfoils performance. In particular, we will validate and verify the transition model results with existing experimental data and high fidelity CFD simulations, such as DNS or LES, and propose a fine-tuning methodology focusing on separation-induced transition. If coupling RANS turbulence models with transition models were reliable, this would bring a significant reduction of computational cost. The cost reduction would allow adopting optimization algorithms based on CFD simulations to improve airfoil design at a low Reynolds number. This fact would have an impact on the performance of micro aerial vehicles, but it would also apply to aircraft flying in exotic conditions, such as the Martian atmosphere, where a low Reynolds number environment is combined with the compressible regime because the speed of sound on the ground is about 240 m/s and propellers rotation speed must be high.

Transition models calibration uses flat plate test cases that are well documented, especially for Reynolds numbers above $5{\cdot}10^4$. The recent interest in low Reynolds number flight requires a revision of such calibrations, as present guidelines may not hold in such conditions. Laminar separation bubbles are of great importance in the low Reynolds number regime as they are, to a great extent, responsible for the non-linearity in the $c_L(\alpha)$ curves of airfoils, which results in a significant deviation, even at small angles of attack (AOA), from the usual expression $c_L = 2\pi\left(\alpha - \alpha_{L=0}\right)$ given by Prandtl's thin airfoil theory. Transition in separation bubbles occurs at much smaller Reynolds numbers than the classical natural transition threshold. Even though Tollmien-Schlichting (T-S) waves amplification is the same as it happens in natural transition, adverse pressure gradients lead to flow separation earlier than natural transition, as they trigger Kelvin-Helmholtz (KH) instability in the separated shear layer, causing its rolling-up into vortices and eventually the transition to turbulence described by Schlichting and Gersten (2016). The turbulent flow efficiently transports momentum towards the wall, thus facilitating the reattachment of the separation bubble as shown in Hain et al. (2009). The presence of a separated flow region alters the effective camber and thickness of the airfoil, influencing the aerodynamic coefficients as presented by Hansen et al. (2014). The LSB position and dimension vary with Reynolds number and AOA. Typically, airfoils in low Reynolds number conditions display trailing edge separation without reattachment at low AOA. As the AOA increases, the adverse pressure gradient grows, and the separation point moves upstream, thus promoting an earlier transition. When the separation point is sufficiently upstream to allow a complete passage to turbulent flow, the flow reattaches near the trailing edge. A further increase of the AOA moves the separation point towards the leading edge until, finally, at a sufficiently large AOA, the adverse pressure gradient is so strong that the turbulent boundary layer completely detaches, producing massive separation and the airfoil stall.

Several authors have analyzed airfoils behavior at low Reynolds numbers both experimentally and numerically. The UIUC Applied Aerodynamics Group UIUC (2020) performed extensive experimental testing on many airfoils, defining guidelines for low Reynolds number airfoil design, which resulted in one of the most popular low Reynolds airfoils, the SD7003. Researchers at NASA Langley McGhee et al. (1988) performed a thorough experimental work on the Eppler 387 airfoil, another popular airfoil for this range of Reynolds numbers. The PIV experimental technique was used in Ol et al. (2005) to compare the SD7003 airfoil separation bubble in three different facilities. More recently, due to the growing interest in Mars flight, a research group based in Japan (Anyoji et al. 2014; Aono et al. 2018) studied various airfoils, including the Ishii airfoil, at Reynolds numbers as low as $2.3{\cdot}10^4$. The first computational approaches are by Eppler and Somers (1980);

Dini and Maughmer (1989), and Drela (1988, 1989), the latter developing Xfoil, a fast, but yet powerful design tool that couples inviscid analysis based on the panel method and integral boundary layer approaches to account for viscous effects. Xfoil includes the e^N method to predict transition, which provides impressive results considering its low computational cost. More sophisticated approaches coupling RANS with the e^N method were presented by Radespiel and Windte (2003) among others. Later on, local correlation-based transition models (LCTM), such as the empirical approach proposed with the γ-Re $_\theta$ model by Menter and Langtry (Menter et al. 2006; Langtry 2006), and the phenomenological approach introduced with the Laminar-Kinetic Energy model (LTEM) by Walters and Cokljat (2008), were developed. The application of the γ-Re $_\theta$ transition model for airfoils operating in the very-low Reynolds number regime is not very well documented in the literature though there are some examples. Babajee (2013) used RANS with the γ-Re $_\theta$ transition model to simulate transition in the suction side of airfoils in the context of low-pressure turbines blades. Choudhry et al. (2015) presents an analysis of long separation bubbles on thick airfoils using both the γ-Re $_\theta$ transition model and the laminar-kinetic energy model. Salimipour (2019) shows a recalibration of the laminar-kinetic energy model comparing the results with the ones provided by the γ-Re $_\theta$ transition model for Reynolds numbers in the very-low Reynolds number regime for a NACA 0012 airfoil. Götten et al. (2019) thoroughly validates the γ-Re $_\theta$ transition model for several airfoils at $Re > 200,000$. Some authors also carried out high-fidelity LES or DNS simulations on classical airfoils at low Reynolds numbers. These techniques do not require a transition model as they can resolve the small turbulence length scales, and thus they can numerically capture transition. Therefore, LES and DNS results are useful references for tuning transition models. Galbraith and Visbal (2010) did extensive Implicit Large Eddy Simulations(ILES) for the SD7003 airfoil at several Reynolds numbers and angles of attack. Uranga et al. (2009) presented additional ILES results for the same airfoil, as did Carton de Wiart and Hillewaert (2012), who completed his work with a DNS. LES simulations were also performed by Anyoji et al. (2014) and Frère et al. (2016) for the Ishii and Eppler 387 airfoils, respectively.

The present study uses the CFD code STAR-CCM+, which offers three transition models coupled with RANS equations, namely (a) Turbulence suppression, (b) γ Transition, and (c) γ-Re $_\theta$ Transition. The turbulence suppression approach requires the knowledge of the transition point and therefore could be used to check the ability of RANS solvers to reproduce separation bubbles Catalano and Tognaccini (2011), but not to determine the transition point. The γ transition model is a one-equation intermittency-based model, which was introduced by Menter et al. (2015) to correct deficiencies in the γ-Re $_\theta$ model with the further advantage of integrating a single equation and of being Galilean invariant. However, the implementation of this model in STAR-CCM+ lacks a separation-induced transition correction constant C_{SEP}, which is necessary to tune the production of turbulent kinetic energy in separated regions controlling in this way the length of the separation bubble. Therefore, in this work, we focus the attention on the γ-Re $_\theta$ transition model.

2 The γ-Re $_\theta$ Transition Model

The γ-Re $_\theta$ transition model, originally proposed by Menter et al. (2006), is a two-equations local correlation-based transition model (LCTM) that solves one transport equation for the intermittency, γ, and another one for the transition onset momentum thickness Reynolds number, $\overline{Re}_{\theta_t}$. It is coupled with the SST k-ω turbulence model, also developed by Menter (1994).

The two transport equations are integrated in time to obtain an effective value for the intermittency, γ_{eff}, which affects the turbulent kinetic energy equation of the $k-\omega$ SST model as follows (Langtry (2006)):

$$\rho\frac{Dk}{Dt} = \nabla\cdot[(\mu+\sigma_k\mu_t)\nabla k)] + \gamma_{eff}P_k - \min[\max[\gamma_{eff},0.1],1]D_k \tag{1}$$

In Eq. (1), P_k and D_k are the original production and destruction terms of the SST k-ω model, respectively. The production term is defined as:

$$P_k = G_k + G_{nl} + G_b \tag{2}$$

Which represent the turbulent production, the non-linear production and the buoyancy production terms respectively. The destruction term is defined as:

$$D_k = \rho\beta^* f_{\beta^*}(\omega k - \omega_0 k_0) \tag{3}$$

where ρ is the density β^* is a model coefficient, f_{β^*} is the free-shear modification factor and ω_0 and k_0 are the ambient turbulence values that counteract decay as shown in Spalart and Rumsey (2007).

The ''effective'' value of the intermittency, γ_{eff}, is calculated as the maximum between the value of the intermittency coming from the transport equation, γ, and that given by the separation-induced transition correction, γ_{sep}:

$$\gamma_{eff} = \max\left(\gamma,\gamma_{sep}\right) \tag{4}$$

where

$$\gamma_{sep} = \min\left(s_1\max\left[0,\frac{Re_v}{3.235Re_{\theta_c}}-1\right]e^{-\left(\frac{R_T}{20}\right)^4},2\right)F_{\theta_t} \tag{5}$$

In Eq. (5), s_1 is a parameter that controls the injection of kinetic energy in the separated region. The latter is the region where the strain-rate (or vorticity-rate) Reynolds number, Re_v, is significantly larger than the critical Reynolds number, Re_{θ_c}, which arises from an empirical correlation as a function of $\overline{Re}_{\theta_t}$. The critical Reynolds number indicates where intermittency first starts to increase in the boundary layer. The scalar value 3.235 represents the ratio between Re_v and Re_{θ_c} when the shape factor, H, is equal to 3.5, that represents the separation point according to Polhausen's method, in a boundary layer subject to an adverse pressure gradient, as shown in Menter et al. (2006).

The STAR-CCM+ implementation, until version 2021.1, uses a value of 2.193 instead of 3.235, as shown in equation Eq. (6).

$$\gamma_{sep} = \min\left(s_1\max\left[0,\frac{Re_v}{2.193Re_{\theta_c}}-1\right]e^{-\left(\frac{R_T}{15}\right)^4},5\right)F_{\theta_t} \tag{6}$$

The value of 2.193 is associated with the maximum ratio between Re_v and Re_{θ_c} in a Blasius profile, and it appears in a first version of the γ-Re $_\theta$ transition model presented in Langtry

et al. (2006). A small change is also present in the damping term decreasing denominator from 20 to 15, and the limiting value of the maximum intermittency increases from 2 to 5. These changes would, in theory, move the transition point slightly upstream and make the transition process faster due to the higher limit of the effective intermittency. Since the version 2021.2, STAR-CCM+ code was updated and the separation-induced transition correction is now the formulation shown in Eq.(5).

The intermittency equation is written as:

$$\rho\frac{D\gamma}{Dt} = \nabla\cdot[(\mu+\frac{\mu_t}{\sigma_\gamma})\nabla\gamma] + P_\gamma - E_\gamma \tag{7}$$

The production term, P_γ, and the destruction term, E_γ, introduced by Langtry (2006) are defined as:

$$P_\gamma = F_{Length}c_{a1}\rho S[\gamma F_{onset}]^{0.5}(1-c_{e1}\gamma) \tag{8}$$

$$E_\gamma = c_{a2}\rho W\gamma F_{turb}(c_{e2}\gamma - 1) \tag{9}$$

In Eqs. (8)–(9),F_{onset} and F_{turb} are trigger functions that activate intermittency production and deactivate relaminarization, respectively. Coefficients c_{a1}, c_{a2}, c_{e1} and c_{e2} are model constants that we set equal to the values originally suggested by Menter et al. (2006). F_{Length} and Re_{θ_c}, the latter embedded in F_{onset}, are empirical correlations expressed as functions of $\overline{Re}_{\theta_t}$. Originally, these correlations were considered proprietary and were not disclosed, thus pushing numerous authors to develop calibrations to fit existing experimental data. For example, Malan et al. (2009) proposed a calibration of the model that was implemented in STAR-CCM+ untill, finally, Langtry and Menter (2009) disclosed the original calibration that is also implemented in the CFD code. Both calibrations are compared in the following section.

The transport equation for the transition onset momentum thickness Reynolds number is defined as:

$$\rho\frac{D\overline{Re}_{\theta_t}}{Dt} = \nabla\cdot[\sigma_{\theta_t}(\mu+\mu_t)\nabla\overline{Re}_{\theta_t}] + P_{\theta_t} \tag{10}$$

Such an equation connects the empirical correlation to the onset criteria in the γ-equation. It accounts for non-local effects due to changes in the freestream turbulence, Tu, and in the pressure gradient at the edge of the boundary layer. In Eq. (10), the production term,P_{θ_t}, is defined as:

$$P_{\theta_t} = c_{\theta_t}\frac{\rho}{t}(Re_{\theta_t} - \overline{Re}_{\theta_t})(1-F_{\theta_t}) \tag{11}$$

where c_{θ_t} is model constant, t is a time scale and F_{θ_t} is a blending function that ensures that inside the boundary layer the production term is turned off and also that the transported scalar $\overline{Re}_{\theta_t}$ matches the value of the empirical correlation $Re_{\theta_t} = f(\lambda_\theta, Tu)$ in the freestream. The original version of the model contained such a correlation that had been previously assessed by other authors such as Abu-Ghannam and Shaw (1980). Langtry (2006) modified the $Re_{\theta_t} = f(\lambda_\theta, Tu)$ correlation to improve results for low turbulence intensity simulations. He noted that when the boundary layer undergoes laminar separation, the model predicted a reattachment location downstream of the actual position in the experiments. The discrepancy was attributed to insufficient production of turbulent kinetic energy in the

separated shear layer when the freestream turbulence intensity is small. Therefore, the correction embedded in Eqs. (4) and (5) was included in the transition model. The former increases the production of turbulent kinetic energy in separated regions, namely allowing the intermittency to exceed unity there.

The γ-Re $_\theta$ transition model is semi-local, as an arbitrary surface has to be defined to indicate the position of the freestream edge, and then these values are diffused into the boundary layer through the transport equation for the transition onset momentum thickness Reynolds number (Eq. (11)).

2.1 Empirical Correlations

As mentioned in the previous section, the empirical correlations that integrate the physics of transition into the model were initially declared proprietary. Suluksna et al. (2009); Malan et al. (2009) performed a calibration of these models for unstructured parallelized codes, which is the default calibration used in STAR-CCM+. In what follows, we will refer to these correlations as to the Saluksna-Juntasaro Calibration. Finally, Langtry and Menter (2009) disclosed the original calibration of the model. There are three empirical correlations needed to close the model. The first one is the critical momentum thickness Reynolds number, $Re_{\theta c}$, which can be considered the point at which the turbulence intensity begins to grow before transition. The second correlation, F_{length}, is designed to control the transition length. And the other correlation needed is the functional relationship between the transition momentum thickness Reynolds number, which represents the transition point observed experimentally, and the freestream turbulence intensity and Thwaites' parameter, $Re_{\theta_t} = f(\lambda_\theta, Tu)$.

In this paper, we will test both calibrations and comment on the effect of the inclusion of the pressure gradient in the case of Menter's correlation. The Suluksna-Juntasaro calibration defines the following correlations for $Re_{\theta c}$ and F_{length}:

$$Re_{\theta c} = min\left(\overline{Re}_{\theta_t}, 0.615\overline{Re}_{\theta_t} + 61.5\right) \tag{12}$$

$$F_{length} = min\left(300, exp(7.168 - 0.01173\overline{Re}_{\theta_t}) + 0.5\right) \tag{13}$$

We used the empirical correlations provided in Langtry and Menter (2009), which are expressed as:

$$Re_{\theta c} = \begin{cases} A_1 + A_2\overline{Re}_{\theta_t} + A_3\overline{Re}_{\theta_t}^2 + A_4\overline{Re}_{\theta_t}^3 + A_5\overline{Re}_{\theta_t}^4, & \overline{Re}_{\theta_t} \leq 1870; \\ B_1 + B_2\overline{Re}_{\theta_t} + B_3\overline{Re}_{\theta_t}^2 + B_4\overline{Re}_{\theta_t}^3, & \overline{Re}_{\theta_t} > 1870 \end{cases} \tag{14}$$

$$F_{length} = F_{length_1}(1 - F_{sublayer}) + 40F_{sublayer} \tag{15}$$

where F_{length_1} is defined as:

$$F_{length_1} = \begin{cases} C_1 + C_2\overline{Re}_{\theta_t} + C_3\overline{Re}_{\theta_t}^2, & \overline{Re}_{\theta_t} < 400; \\ D_1 + D_2\overline{Re}_{\theta_t} + D_3\overline{Re}_{\theta_t}^2 + D_4\overline{Re}_{\theta_t}^3, & 400 \le \overline{Re}_{\theta_t} < 596; \\ D_1 + D_2\left(\overline{Re}_{\theta_t} - D_3\right), & 596 \le \overline{Re}_{\theta_t} < 1200; \\ E, & \overline{Re}_{\theta_t} \ge 1200 \end{cases} \tag{16}$$

and $F_{sublayer}$ is defined as:

$$F_{sublayer} = exp\left[-\left(\frac{\omega d^2}{200\nu}\right)^2\right] \tag{17}$$

The values of the numerical coefficients A_i, B_i, C_i, D_i, and E can be found in Langtry and Menter (2009). These correlations are significantly more complex than those used by Suluksna-Juntasaro including both higher-order polynomials and differentiation for different turbulence intensities conditions implicitly through $\overline{Re}_{\theta_t}$. The correlations used in both cases for Re_{θ_t} are those proposed in Langtry and Menter (2009):

$$Re_{\theta_t} = \begin{cases} \left(1173 - 589.428Tu + \dfrac{0.2196}{Tu^2}\right)F(\lambda_\theta), & Tu < 1.3\%; \\ 331.5(Tu - 0.5658)^{-0.671}F(\lambda_\theta), & Tu > 1.3\% \end{cases} \tag{18}$$

The only difference is that the Suluksna-Juntasaro calibration sets $F(\lambda_\theta)$ to 1, so that the correlation is independent from the pressure gradient, while Langtry and Menter (2009) defines $F(\lambda_\theta)$ as:

$$F(\lambda_\theta) = \begin{cases} 1 - \left(-12.986\lambda_\theta - 123.66\lambda_\theta^2 - 405.689\lambda_\theta^3\right)e^{-\left(\frac{Tu}{1.5}\right)^{1.5}}, & \lambda_\theta < 0; \\ 1 + 0.275\left(1 - e^{-35\lambda_\theta}\right)e^{\left(\frac{-Tu}{0.5}\right)}, & \lambda_\theta > 0 \end{cases} \tag{19}$$

Thwaites' parameter,λ_θ, is defined as:

$$\lambda_\theta = \frac{\theta^2}{\nu}\frac{dU}{ds} \tag{20}$$

but the boundary layer transition momentum thickness is not calculated as an integral quantity due to the great cost that this would generate for unstructured parallelized codes. This quantity is estimated locally from the value Re_{θ_t}. Therefore equation (18) must be solved iteratively.

3 Numerical Simulation and Validation

3.1 Physical/mathematical Model and Numerical Method

The physical/mathematical model used to simulate the flowfield is based on the compressible unsteady Reynolds-Averaged Navier Stokes (URANS) equations. As already mentioned, the turbulence model is the two-equations SST k-ω model, which is coupled with

the two-equations γ-Re $_\theta$ transition model. The implementation is the one offered by the commercial CFD software STAR CCM+, in particular version 14.06.12. The calculation of inviscid fluxes adopts a second-order reconstruction scheme combined with Roe's scheme, whereas the evaluation of viscous fluxes uses a second-order central difference. Although the formation of separation bubbles is an unsteady process characterized by vortex shedding as shown in Galbraith and Visbal (2010), time-resolved simulations are not always required. The mean separation bubble is usually steady so that we could use a RANS solver. However, in situations close to the bubble bursting, the periodic vortex shedding is intense, and the mean values of lift and drag obtained with unsteady simulations significantly differ from the values provided by the steady solver. In this regard, Pauley et al. (1990) suggests that the bursting of the bubble, described for the first time in Gaster (1967), is associated with an averaged vortex shedding. The URANS simulations shown in Sect. 5 employ an implicit second-order time integration scheme, with a time step of $10^{-5}s$. The time step length ensures that the vortex shedding regime is resolved and allows for the convergence of the inner solver, which runs for ten iterations every time step.

3.2 Computational Domain and Boundary Conditions

The adopted computational domain is visible in Fig. 1. Its extension is about 1000 chords in the streamwise direction (400 upstream and 600 downstream) and 600 chords (at the outlet section) in the transversal direction. We chose such a large domain to minimize the influence of the far-field boundary conditions, as recommended for the NACA 0012 test case in the NASA Turbulence Modeling Resource (Rumsey (2014)). We enforce the freestream, inflow boundary conditions (Mach number, and static pressure and temperature) on a parabolic-shaped ''inflow'' surface, and we impose the freestream pressure on the ''ouflow'' flat surface normal to the freestream direction. No-slip, adiabatic wall conditions are set on the airfoil surface. As we will show in the next section, the freestream is always aligned with the x-axis, and the airfoil is rotated (and the grid is re-meshed) to account for changes in the angle of attack. The boundary conditions for the turbulent kinetic energy and the specific dissipation rate are null wall flux and a fixed freestream value. The boundary conditions for intermittency are a value of 1 at the freestream and

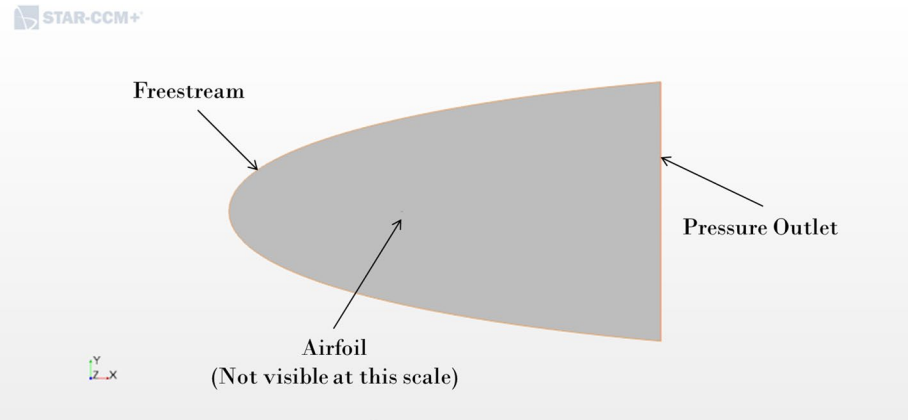

Fig. 1 Fluid domain and boundary conditions

zero wall flux. The boundary conditions for the transition momentum thickness Reynolds number derive from (18) in the freestream (without using the pressure gradient correction) and consist in a null flux at the walls.

3.3 Grid Generation and Refinement Analysis

We built the computational meshes using the automated, unstructured polyhedral mesh generation software embedded in STAR-CCM+ in combination with a prism layer mesh in the near-wall region. As suggested in Peric and Ferguson (2005), polyhedral cells can potentially speed up simulations convergence as information spreading might be enhanced by having more neighboring cells than quadrilateral or triangular grids. That is a positive feature for low-Reynolds numbers simulations that incorporate a transition model since the former usually suffer from slow convergence rates. Since the computational domain is huge, an adaptive mesh refinement (AMR) strategy has been implemented based on pressure and velocity gradients to reduce the number of cells where they are not needed, for example, in the far-field region, where gradients are almost zero. In addition, the AMR approach is quite useful in the low-Reynolds number regime, where the flowfield can change drastically with the angle of attack, moving from fully attached boundary layer situations to the formation of separation bubbles or even massive separations. Fig. 2 shows an example of the effect of the AMR strategy. One can see that the grid is quite fine near the leading edge due to the large local pressure and velocity gradients, but also in the separated shear layer and wake regions due to the large velocity gradients. The refined area in the central-rear region of the suction side is associated with the reattachment of a separation bubble. A prism layer with $y^+ < 1$ helps to properly resolve the wall region, as indicated for this transition model by Langtry (2006). The grid independence study shown in Table 3 has been carried out for airfoil SD7003 at Reynolds 60,000 and $\alpha = 4^o$. Three different grid generation strategies, namely coarse, medium and fine, have been defined for both the prism layer and polyhedral mesh as shown in Tables 1 and 2. From now on, we will adopt the medium/medium grid combination, as it is a good compromise between computational cost and the correct determination of aerodynamic coefficients and flowfield features. It is important to point out that the number of cells associated with AMR strategies is not constant and can vary up to a factor of 2 when massive separation is present, especially at high angles of attack and noticeably low Reynolds numbers.

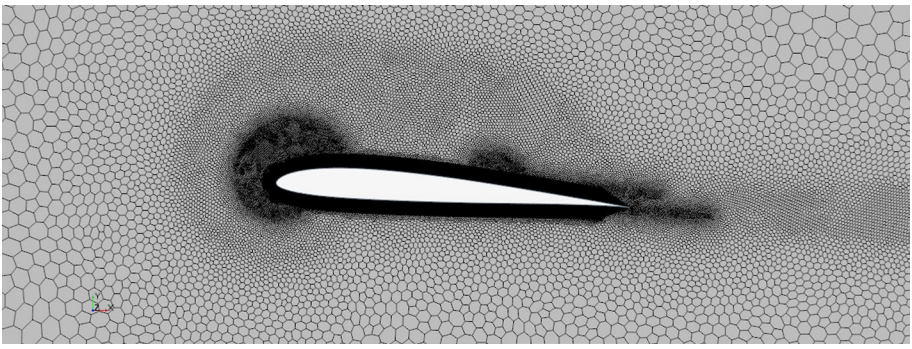

Fig. 2 Medium/Medium grid for airfoil SD7003 at $\alpha = 4^o$ and Re=60,000

Table 1 AMR grid size specifications

Grid	Minimum cell size(%c)	Maximum cell size(%c)
Coarse	0.4	4000
Medium	0.3	3000
Fine	0.2	2000

Table 2 Prism Layer specifications

Grid	Chordwise spacing(%c)	No. of Layers	Wall Cell Thickness(%c)
Coarse	0.6	25	0.004
Medium	0.3	50	0.004
Fine	0.15	75	0.004

Table 3 Grid convergence study for airfoil SD7003 at Re=60,000, $\alpha = 4^o$

Grid/Prism Layer	No. of cells	$\frac{x_{sep}}{c}$	$\frac{x_{re}}{c}$	C_l	C_d
Medium/Coarse	43,774	0.176	0.781	0.6025	0.02730
Coarse/Medium	58,510	0.181	0.742	0.6007	0.02591
Medium/Medium	69,834	0.181	0.741	0.6020	0.02585
Fine/Medium	103,480	0.181	0.741	0.6021	0.02581
Medium/Fine	135,581	0.181	0.742	0.6047	0.02580
Fine/Fine	167,084	0.182	0.741	0.6016	0.02574

3.4 Freestream Turbulence Conditions

Transition is very sensitive to freestream turbulence conditions. In the γ-Re$_\theta$ model, sensitivity to freestream turbulence intensity is obtained through the empirical correlations defined in Eqs. (18) and (19). Turbulence intensity can be measured experimentally, but another variable associated with the length scale of turbulence is needed, for example, the specific dissipation rate, ω, whose determination is challenging and whose value is not always available in existing data. In addition, computational domains used in CFD simulations are usually large to reduce the influence of the boundary conditions, but since turbulence intensity decays as the flow approaches the body, the effective value of turbulence intensity in front of the airfoil can be significantly smaller than the value given at the numerical inlet boundary. A solution to this problem is increasing the turbulence intensity at the computational inflow to match the experimental value at the leading edge, as shown in Choudhry et al. (2015). Provided that turbulence intensity and turbulent viscosity ratio near the airfoil are known from experiments, the following equations provide an initial guess for their freestream ''inlet'' values (Siemens Digital Industries Software (2019)):

$$Tu = (Tu)_{inlet}\left(1 + \frac{0.1242x\rho U_\infty (Tu)^2_{inlet}}{\mu(TVR)_{inlet}}\right)^{-0.5435} \tag{21}$$

$$TVR = (TVR)_{inlet}\left(1 + \frac{0.1242x\rho U_{\infty}(Tu)^2_{inlet}}{\mu(TVR)_{inlet}}\right)^{-0.087} \tag{22}$$

The turbulent viscosity ratio and turbulence intensity can be defined using turbulent kinetic energy and the specific dissipation rate as shown in the following equations:

$$Tu = \frac{\sqrt{\frac{2}{3}k}}{U} \tag{23}$$

$$TVR = \frac{k}{\omega\mu} \tag{24}$$

An issue related to freestream turbulence conditions is that meshes are usually coarse near freestream boundaries, which prevents an accurate resolution of the freestream turbulence decay. In connection to this point, Menter et al. (2015) stated that inlet values for the eddy viscosity ratio affect the turbulence intensity decay and that this affects the transition location. Spalart and Rumsey (2007) suggested the introduction of a source term in the turbulent kinetic energy equation that maintains constant the value of the turbulence intensity, thus overriding the previously mentioned issues. This option is available in STAR-CCM+, and it was adopted in this study, allowing to set the turbulence intensity at the inlet to the actual value measured in the experiments. In this way, the effect of the eddy viscosity ratio should not be very significant because turbulence intensity stays artificially constant. We tested the hypothesis by performing a sensitivity analysis by varying the turbulence conditions at the inlet. We found out that the effect of the TVR is almost negligible as long as the latter is large enough to avoid the turbulence model staying dormant. The magnitude of the minimum TVR value tends to increase with freestream turbulence intensity. Figure 3 shows that, for small values of inlet TVR, the boundary layer remains laminar, and the flow around the airfoil is inconsistent. A TVR equal to 1 seems to work adequately, despite being higher than the value suggested by Rumsey and Spalart (2009) for the SST model. The explanation is that probably the values recommended in Rumsey and Spalart (2009) were intended for the use of the SST turbulence model to predict transition without transition model, setting the freestream turbulence conditions in such a way that the model remains dormant near the leading edge and then it switches on mimicking the transition.

Concerning the freestream value of turbulence intensity, Schlichting and Gersten (2016) states that, based on experimental data, the effect of Tu values smaller than 0.1% is irrelevant. On the other hand, Langtry (2006) sets $Tu = 0.027\%$ as the lower limit for numerical stability. Therefore, selecting Tu between 0.027% and 0.1% at freestream appears a reasonable choice for comparisons with LES simulations that use an ideal freestream to reduce computational costs. Unfortunately, the correlation $Re_{\theta_t} = f(Tu, \lambda_\theta)$ suggested by Langtry (2006) and shown in Eq. (18) is in fact sensitive to Tu values in this range, as shown in Table 4. In summary, despite some authors using the freestream Tu as a tuning parameter to fit existing experimental data or LES simulations, the authors believe that the limiting value of Tu should not be larger than 0.1%. In fact, since the correlation for Re_{θ_t} in Eq. (18) is based on many experimental data obtained at different turbulence intensities, using Tu as a tuning parameter for the transition model would not be consequential. The simulations presented in this paper employ a freestream turbulence intensity of 0.03% to allow a reasonable comparison with LES

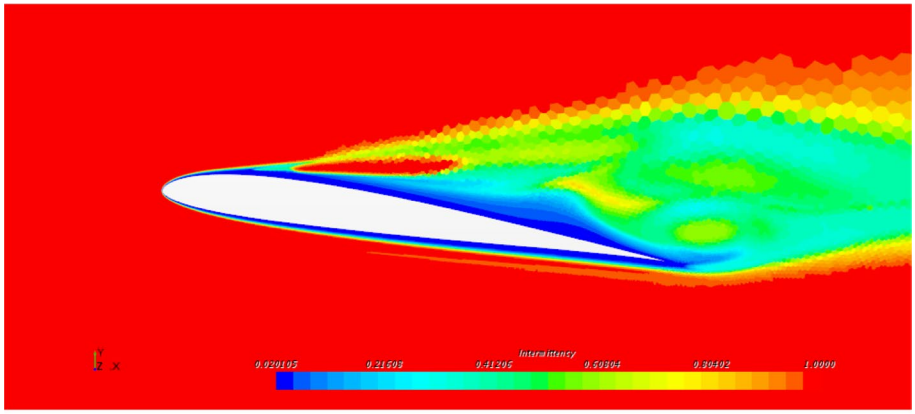

(a) TVR=0.01

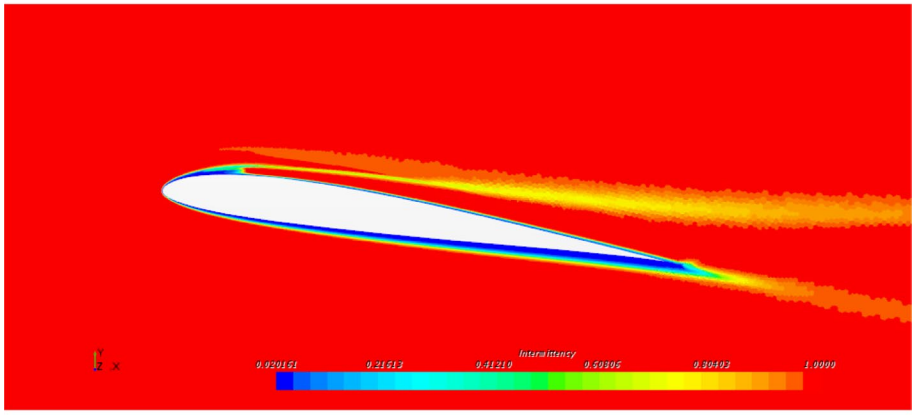

(b) TVR=1.00

Fig. 3 Intermittency contours for airfoil SD7003 at $\alpha = 8^o$, Re=60, 000, $Tu = 0.43\%$

simulations, which assume an ideal freestream. The turbulent viscosity ratio is equal to 1.

3.5 Test Case: Low Reynolds Number Airfoil SD7003

Tables 5 and 6 contain the performance coefficients and the separation and reattachment locations for two different angles of attack of the low Reynolds number airfoil SD7003 calculated with both Suluksna-Juntasaro(S-J) and Menter's calibrations compared with available experimental data and LES simulations performed by Ol et al. (2005) and Galbraith and Visbal (2010), respectively. There are noticeable differences between calibrations and the Menter calibration performs significantly better. However, it is not sure that this trend can be extrapolated to other airfoils, as larger thicknesses and curvatures could introduce differences associated with the pressure gradient correction included in Menter's correlation. When a laminar separation bubbles forms, the skin friction and pressure distributions

Table 4 Sensitivity to turbulence inflow conditions. Airfoil SD7003, Re=60,000, $\alpha = 8^o$

Tu(%)	TVR	C_l	C_d
0.03	0.001	0.9188	0.04105
0.08	0.001	0.7418	0.04285
0.43	0.001	−0.0318	0.02895
0.03	0.01	0.9223	0.04095
0.08	0.01	0.9291	0.03911
0.43	0.01	−0.0060	0.02986
0.03	0.1	0.9225	0.04090
0.08	0.1	0.9304	0.03909
0.43	0.1	0.9299	0.03709
0.03	1	0.9225	0.04089
0.08	1	0.9304	0.03908
0.43	1	0.9294	0.03707
0.03	10	0.9225	0.04090
0.08	10	0.9304	0.03908
0.43	10	0.9396	0.03706

Table 5 Aerodynamic coefficients and LSB characteristics for different models. Re=60,000, $\alpha = 4^o$

	$\frac{x_{sep}}{c}$	$\frac{x_{tr}}{c}$	$\frac{x_{re}}{c}$	C_l	C_d
Menter	0.202	0.518	0.660	0.600	0.0221
Suluksna-Juntasaro	0.184	0.53	0.743	0.600	0.0257
LES(Galbraith and Visbal 2010)	0.23	0.55	0.65	0.59	0.021
PIV(Ol et al. 2005)	0.18	0.47	0.58	–	–
DNS(Carton de Wiart and Hillewaert 2012)	0.209	–	0.654	0.602	0.0196

Table 6 Aerodynamic coefficients and LSB characteristics for different models. Re=60,000, $\alpha = 8^o$

	$\frac{x_{sep}}{c}$	$\frac{x_{tr}}{c}$	$\frac{x_{re}}{c}$	C_l	C_d
Menter	0.035	0.158	0.280	0.922	0.0409
Suluksna-Juntasaro	0.037	0.178	–	0.868	0.0557
LES(Galbraith and Visbal 2010)	0.04	0.18	0.28	0.92	0.043

on the suction side have a very characteristic behavior as described in Selig (2003) which can be appreciated in Figs. 4–5. The pressure distribution shows a plateau with an approximately constant value equal to the pressure at the separation point. When the flow reattaches, the pressure recovers and approaches the inviscid distribution. On the other hand, the skin friction distribution displays an initial rapid decrease due to the adverse pressure gradient that triggers the boundary layer separation. Then, it reaches a negative value close to zero, associated with an almost stagnant reversed flow. The separated shear layer becomes unstable and starts to shed vortices. The impingement of these vortices on the

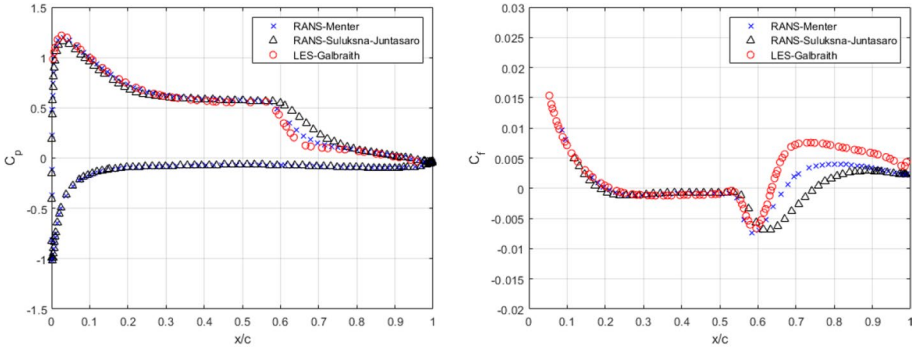

(a) Pressure coefficient. **(b)** Skin friction coefficient.

Fig. 4 Pressure and skin friction coefficients at the suction side of airfoil SD7003 at Re=60,000, $\alpha = 4^o$

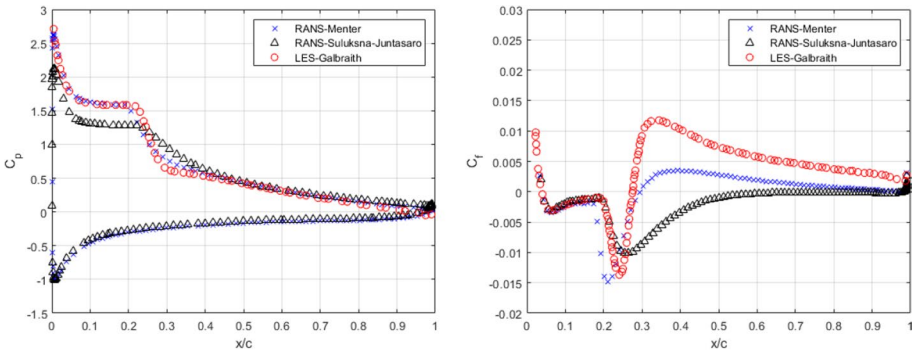

(a) Pressure coefficient. **(b)** Skin friction coefficient.

Fig. 5 Pressure and skin friction coefficients at the suction side of airfoil SD7003 at Re=60,000, $\alpha = 8^o$

airfoil surface creates high skin friction regions, and the boundary layer reattaches. By time-averaging this process, we recover the usual representation of the separation bubble first described by Gaster (1967), which generates a rapid descent of the skin friction and posterior reattachment of the boundary layer. Transition to turbulence occurs in the separated shear layer triggered by K-H instability as described in Burgmann et al. (2008). PIV measurements by Park et al. (2020) demonstrate that transition in a laminar separation bubble occurs in a finite length and that the interval included between the transition onset and the transition completion contains the end of the pressure plateau. For comparison purposes, we define the transition location shown in Tables 5 and 6 as the point where the skin friction starts to drop, as these locations agree better with Galbraith and Visbal (2010) and they probably represent the onset of transition described in Park et al. (2020).

Figures 4–5 show the comparison of the friction and pressure coefficient between RANS simulations and LES simulations performed by Galbraith and Visbal (2010) at a Reynolds number of 60,000 and an angle of attack of 4^o and 8^o respectively. One can see that Menter's correlation performs much better, reproducing the pressure coefficient almost perfectly in both cases. However, there are some evident differences between the friction coefficients. The first is that Menter's correlation produces an early transition, which is

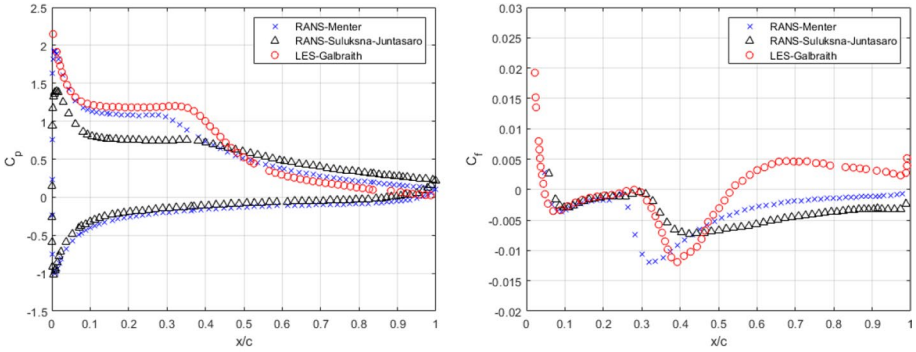

(a) Pressure coefficient. **(b)** Skin friction coefficient.

Fig. 6 Pressure and skin friction coefficients at the suction side of airfoil SD7003 at Re=30,000, $\alpha = 8^o$

Table 7 Aerodynamic coefficients and LSB characteristics for different models and empirical correlations. Re=30,000, $\alpha = 8^o$

	$\frac{x_{sep}}{c}$	$\frac{x_{tr}}{c}$	$\frac{x_{re}}{c}$	C_l	C_d
Menter	0.054	0.250	–	0.828	0.070
Suluksna-Juntasaro	0.066	0.303	–	0.71	0.086
LES(Galbraith and Visbal 2010)	0.05	0.25	0.53	0.89	0.070

more evident for 8^o, characterized by a sudden drop in the friction coefficient. It is also appreciable that the value of the friction coefficient obtained by LES after reattachment is much larger than the value obtained by RANS. The S-J calibration shows negative values of the friction coefficient, evidencing the lack of reattachment of the flow. The transition model cannot produce a sufficiently large value of the friction coefficient after reattachment for these Reynolds numbers and freestream turbulence conditions. Such behavior could lead to enhanced turbulent separation and possibly to an early stall. Figure 6 shows that, for a considerably lower Reynolds number, this effect is even more evident, and the skin friction coefficient plot doesn't indicate the presence of a reattachment point. Table 7 shows that lift and drag coefficients calculated with Menter's correlation are not far away from those predicted by Galbraith and Visbal (2010) and the reason for this is possibly that the prediction of the separation bubble is accurate, looking at the plateau present in the pressure distribution, even though it is not perfectly closed due to the greater importance of pressure drag compared to the shear drag. It is also clear that the prediction capabilities of the model deteriorate for decreasing Reynolds numbers and increasing angles of attack.

In Sect. 2 we described the two different formulations (Eqs. (6) and (5)) designed to increase the intermittency value above 1. That is necessary to compensate for the transition model's intrinsic lack of turbulent kinetic energy production in case of separation-induced transition, as explained in Langtry (2006). The first formulation (Eq. (6)), was introduced by Menter et al. (2004) and was later updated by Langtry and Menter (2009) (Eq. (5)) to adjust the slightly premature transition observed in the tested cases. STAR-CCM+ implemented Eq. (6) until version 2021.1 and updated it to Eq. (5) since version 2021.2. We tested both separation-induced transitions, as shown in Table 8. The original correction performs much better if one compares the airfoil aerodynamic coefficients with

Table 8 Aerodynamic coefficients and LSB characteristics for different separation-induced transition corrections using Menter correlations. SD7003 airfoil, Re=60,000, $\alpha = 4^o$

	$\frac{x_{sep}}{c}$	$\frac{x_{tr}}{c}$	$\frac{x_{re}}{c}$	C_l	C_d
Menter-Original (Eq.(6))	0.202	0.518	0.660	0.600	0.0221
Menter-Updated (Eq.(5))	0.185	0.535	0.769	0.603	0.0259
LES(Galbraith and Visbal 2010)	0.23	0.55	0.65	0.59	0.021

those reported by Galbraith and Visbal (2010). Regarding the separation bubble characteristics captured by the new formulation (Eq. (5)), the bubble length is too large, whereas the transition point is slightly delayed and not too far from the high fidelity simulations. The slightly delayed transition was expected due to the modification of the 2.193 constant in Eq. (6) to 3.235 in Eq. (5). To explain why the reattachment location is downstream compared to the original correction, we present the effective intermittency in the flow field in Fig. 7. The decrease in the limiting value of this quantity from 5 to 2 reduces the turbulence kinetic energy production and, therefore, considerably delays reattachment. These results suggest that a hybrid correction, which postpones transition using the value of 3.235

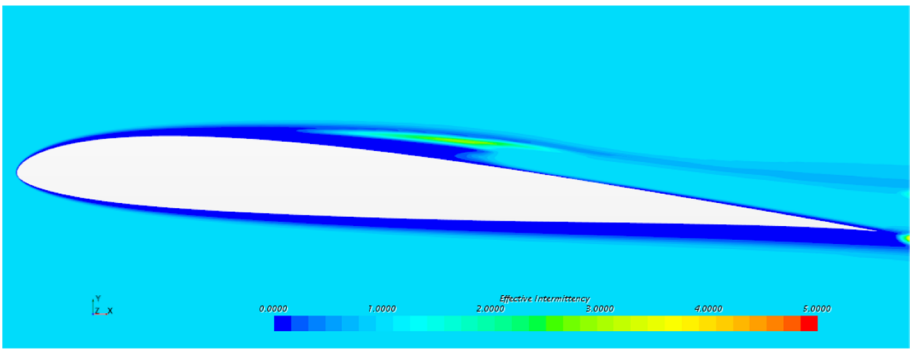

(a) Original separation-induced transition (Eq.(6)).

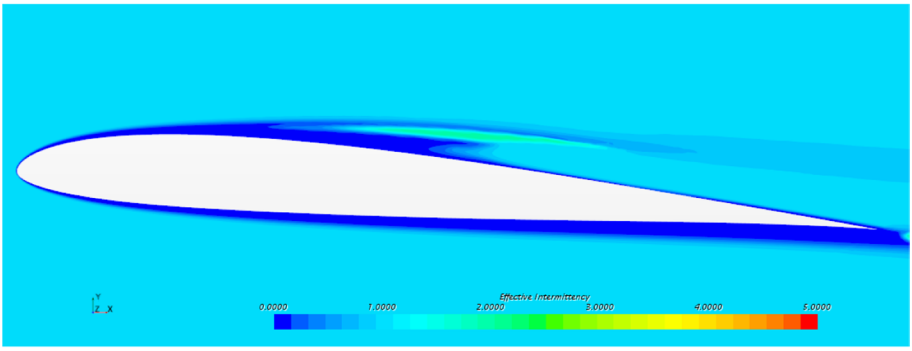

(b) Updated separation-induced transition (Eq.(5)).

Fig. 7 Effective intermittency around airfoil SD7003 at Re=60,000, $\alpha = 4^o$

and employs a faster turbulence kinetic energy production mechanism, could outperform the previous two corrections. In the rest of the paper, we will use the original correction (Eq. (6)) as it works better than the updated correction (Eq. (5)) in the considered regime. Another interesting conclusion we can draw from Fig. 7 concerns the relatively high values of the effective intermittency in separated regions. In the case of the original separation-induced correction (Eq. (6)), the effective intermittency reaches values well above 3. Thus, when the flow separates, the production term can be over 300% larger than in the natural or bypass transition, making the solution little sensitive to F_{length} and Re. That is probably the reason for the apparent independence of the results from the choice of Suluksna-Juntasaro's or Menter's calibration when the pressure gradient correction is unused, as discussed in the next section.

4 Transition Model Fine-Tuning for Low Reynolds Numbers

The previous section shows two main flaws of the γ-Re $_\theta$ transition model. One is the low wall shear stress predicted after transition, which will eventually arise in a premature stall. The second one is the early transition and reattachment at intermediate angles of attack (6° to 8°), as suggested by the lower values of the drag coefficient in comparison to the LES results, which descend from a smaller size of the separation bubble. This can be seen in Table 6 and Fig. 5 for $\alpha = 8^o$, but it is more evident at 6 degrees as shown in Table 9. Even though the reattachment locations look close or even downstream in the case of 8 degrees, the slower rise of the skin friction coefficient due to this transition model slightly delays reattachment, and at that chord position, the pressure has almost completed its recovery towards the inviscid distribution. These two issues require turbulence intensity production to be tuned specifically depending not only on the position on the suction side of the airfoil but also on the angle of attack. This fact makes a simple tuning of the model using constant values of the parameters a difficult task. Another important consideration is that the model doesn't account for 3D effects that could potentially be responsible for the previously mentioned discrepancies. Figure 8 shows an attempt to adjust the parameter s_1 to fit aerodynamic coefficients provided by Galbraith and Visbal (2010) using Menter's calibration. Menter et al. (2006) included such a parameter to increase the turbulence intensity produced after transition, controlling in this way the size of the bubble and the drag coefficient simply and effectively. However, Fig. 8 clearly shows that it is not possible to accurately fit results for different angles of attack using a constant value of s_1 especially for the highest angle of attack. In the light of what we saw in the previous section, such an effect could even be larger at lower Reynolds numbers. Observations in this direction were presented by Corral and Gisbert (2010), who realized that a constant value of s_1 was not enough and established a relationship between s_1 and $\overline{Re}_{\theta_t}$. The noticeably low value of s_1 required for $\alpha = 6^o$ puts in evidence the previously mentioned early reattachment for intermediate angles of attack. That indicates that also transition happens too early, probably for two reasons. The first cause is that the pressure gradient correction noticeably reduces the momentum thickness transition Reynolds number. The second reason is that the original separation-induced transition correction starts producing turbulent kinetic energy too early, as shown in the previous section, Malan et al. (2009) suggest that the pressure gradient correction introduced by Menter in Eq. (19) produces a double accounting of pressure gradient effects on transition momentum thickness because the turbulence intensity will grow naturally in the presence of an adverse pressure gradient. Therefore the pressure gradient

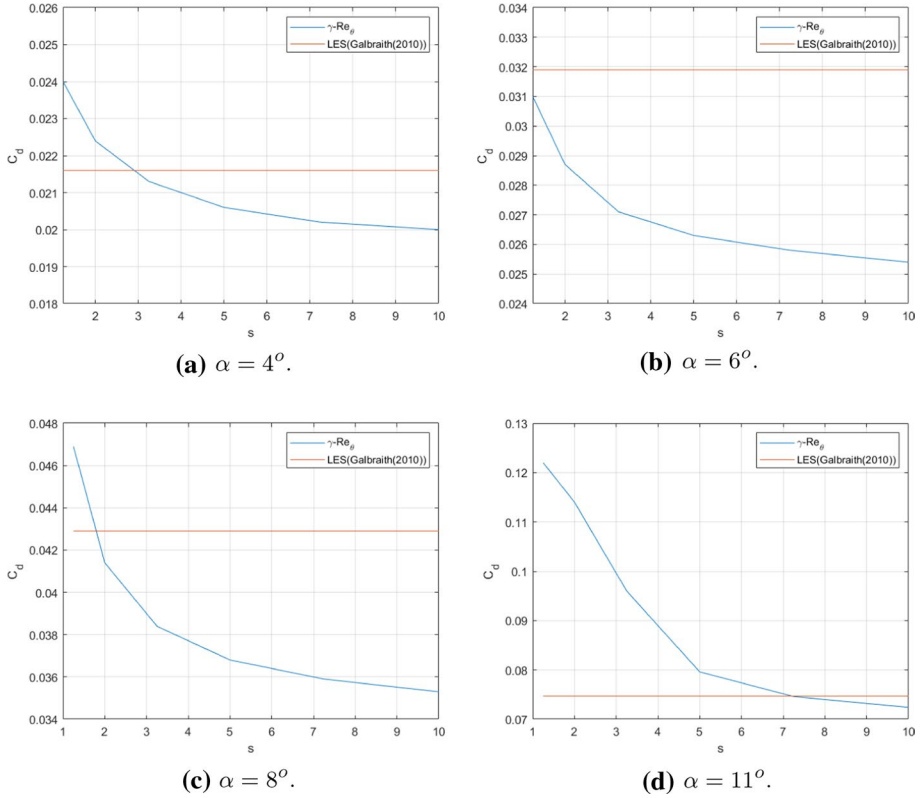

(a) $\alpha = 4^o$. **(b)** $\alpha = 6^o$.

(c) $\alpha = 8^o$. **(d)** $\alpha = 11^o$.

Fig. 8 Drag coefficient of airfoil SD7003 as a function of s_1 at Re=60,000

effects are being taken into account both implicitly by the previously explained mechanism and explicitly through Eq. (19). Such a double accounting could cause the premature transition predicted by Menter's correlations. At the same time, the relatively high value of s_1 required for $\alpha = 11^o$ shows that, at high angles of attack, the small skin friction coefficient calculated by the model after the transition is not sufficient for keeping the turbulent boundary layer attached as predicted by the LES simulations. That causes a wide separation on the suction side with a consequent rise in the drag coefficient and a decrease in the lift coefficient, as is typical in stalled airfoils. Leaving aside the highest angle of attack, the original value of $s_1 = 2$ seems to be an acceptable compromise to fit the drag coefficient values for angles of attack of 4, 6, and 8 degrees.

In the previous section, we showed that the Suluksna-Juntasaro calibration, which does not include the pressure gradient correction, moves the transition point slightly downstream and that the computed values agree better with Galbraith's results, Galbraith and Visbal (2010). However, the reattachment point position is excessively downstream, which increases the length of the bubble and thus the drag coefficient. To find a compromise between the Suluksna-Juntasaro and the Menter calibration, we tested the first for different values of s_1. Table 10 shows that, by increasing the s_1 value to 6, the Suluksna-Juntasaro calibration still predicts well the transition location, and, at the same time, the reattachment position and drag coefficient values get close to those predicted by the Menter's calibration.

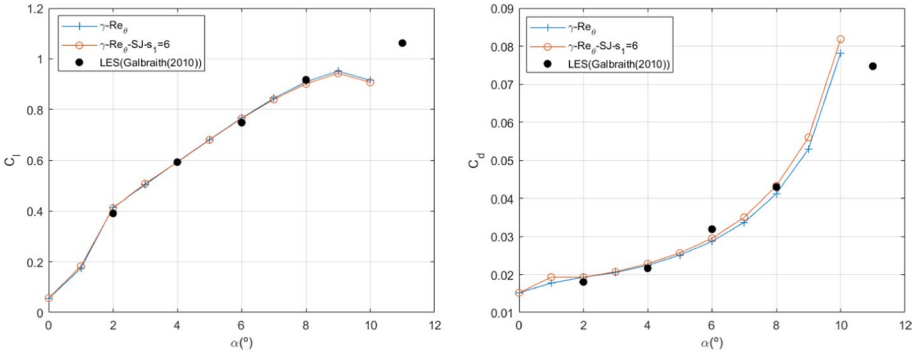

(a) Lift coefficient. **(b)** Drag coefficient.

Fig. 9 Lift and drag coefficients of airfoil SD7003 at Re = 60,000

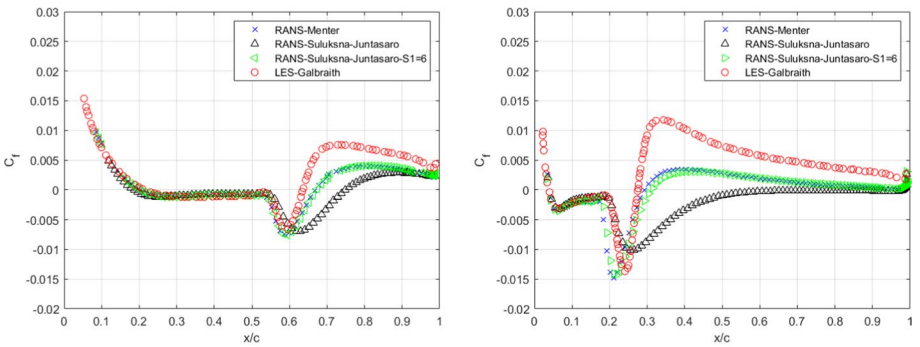

(a) $\alpha = 4^o$. **(b)** $\alpha = 8^o$.

Fig. 10 Skin friction coefficients at the suction side of airfoil SD7003 at Re=60,000

Table 9 Aerodynamic coefficients and LSB characteristics for different models and empirical correlations. Re=60,000, $\alpha = 6^o$

	$\frac{x_{sep}}{c}$	$\frac{x_{tr}}{c}$	$\frac{x_{re}}{c}$	C_l	C_d
Menter	0.098	0.317	0.44	0.767	0.0287
LES(Galbraith and Visbal 2010)	0.11	0.34	0.45	0.748	0.0319

Table 10 Aerodynamic coefficients and LSB characteristics for different models and s_1 values. SD7003 airfoil, Re=60,000, $\alpha = 4^o$

	$\frac{x_{sep}}{c}$	$\frac{x_{tr}}{c}$	$\frac{x_{re}}{c}$	C_l	C_d
Menter	0.202	0.518	0.660	0.600	0.0221
Menter-ZPG	0.184	0.544	0.767	0.597	0.0264
Suluksna-Juntasaro-s_1=2	0.184	0.530	0.743	0.600	0.0257
Suluksna-Juntasaro-s_1=6	0.202	0.536	0.680	0.593	0.0228
LES(Galbraith and Visbal 2010)	0.23	0.55	0.65	0.59	0.021

Table 10 also highlights that the Menter's correlation without the pressure gradient correction (ZPG) behaves like the Suluksna-Juntasaro calibration. Figures 9–10 evidence that this is true not only for $\alpha = 4^o$ and also that $s_1 = 6$ in the Suluksna-Juntasaro calibration provides similar results, as the Menter's calibration, which uses the pressure gradient correction, for all tested angles of attack. That indicates that the pressure gradient and the separation-induced corrections play a similar role. Either directly or indirectly, they both enhance the production of turbulence intensity in separated regions. The main drawback of using the pressure gradient correction is that the Menter calibration predicts transition upstream than the S-J correlation. As mentioned earlier, this is possibly related to a double accounting of the pressure gradient effects. The Suluksna-Juntasaro calibration, on the other hand, produces more turbulence kinetic energy because of the increased value of the s_1 parameter and, despite starting slightly later, predicts transition and reattachment closer to the LES-predicted positions compared to the Menter's correlation. This analysis allows for several conclusions. The first is that the pressure gradient correction presented in Menter's correlations causes a slightly premature transition. A second conclusion is linked to the observation that Menter's correlation without the pressure gradient correction and Suluksna-Juntasaro correlation produce very similar results. This fact may indicate that for this type of transition, simple $Re_{\theta c}$ and F_{length} correlations (such as S-J's) perform as well as complex and general correlations (such as Menter's) and therefore that the priority should be fine-tuning the separation-induced transition correction. Thus, even though the s_1 constant is a very effective way of fixing the length of the separation bubble for specific cases, it seems clear that setting it as a constant makes it very difficult to fit a broad range of angles of attack with different kinds of separation bubbles. Furthermore, introducing a second parameter, independent of s_1, would be functional in controlling the position and length of the separation bubble simultaneously.

5 Enhanced Performance Predictions using the Unsteady Solver

The γ-Re $_\theta$ transition model essentially switches from laminar solutions when the intermittency is close to zero to turbulent solutions when the intermittency approaches the unit value. In the previous chapters, we focused on transition and the capturing of separation bubbles. At Reynolds numbers around 60,000, only angles of attack below 1^o show a fully laminar suction side, but these angular values are below the range of interest for rotor and wing applications, which usually work around the optimum angle of attack. However, the range of angles of attack for which the flow remains laminar becomes broader for decreasing Reynolds numbers, and at Re=20,000 can arrive up to 3^o to 4^o. The authors pointed out in Carreño Ruiz et al. (2022) that, in some cases, steady laminar solutions display some differences compared with time-accurate solutions of the Navier-Stokes(N-S) equations. At small angles of attack, steady-state N-S solutions predict a stable, separated region behind the airfoil trailing edge, but time-accurate simulations indicate a vortex shedding regime. The periodic vortex shedding generates an average lift enhancement due to the low pressure generated by these high-velocity regions on the suction side. Figure 11 shows a comparison between the velocity magnitude around the airfoil SD7003 at Re=23,000 and $\alpha = 2^o$. The vortex shedding generated near the trailing edge affects the velocity magnitude distribution around the airfoil and thus its performance, as shown in Table 11. For higher angles of attack, as the intermittency begins to increase, the averaging introduced by the turbulence

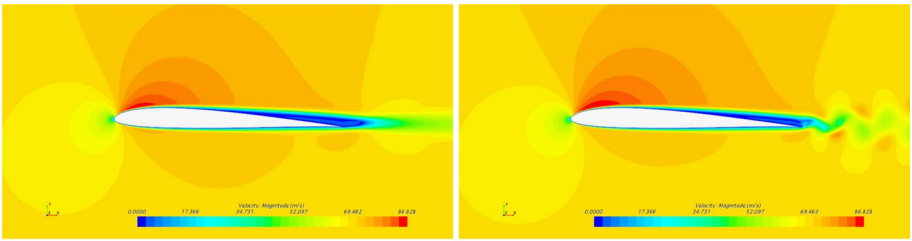

(a) Steady Solver. **(b)** Unsteady Solver.

Fig. 11 Instantaneous velocity magnitude around airfoil SD7003 at $\alpha = 2^o$ and Re=23,000

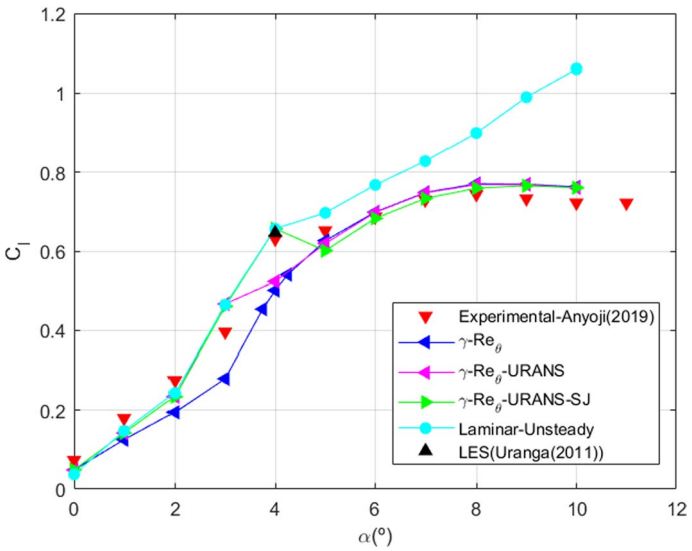

Fig. 12 Lift coefficient of airfoil SD7003 at Re=23,000 for different solvers compared with experimental (Anyoji and Hamada 2019) and high fidelity numerical data (Uranga 2010)

Table 11 Aerodynamic coefficients obtained using the steady and the unsteady solver. Re=23,000, $\alpha = 2^o$

Solver	C_l	C_d
Steady	0.193	0.0273
Unsteady	0.237	0.0283
Difference(%)	+22.80	+3.66

model dampens the instability, and the steady and unsteady solutions converge. Figure 12 summarizes well the influence of using an unsteady solver. Between 0^o to 3^o, one can see that all unsteady simulations provide almost identical results, including laminar simulations. At 4^o, we notice that using Menter's calibration, the unsteady solver with transition model shows a noticeable drop in the lift coefficient compared to the other numerical and experimental data. That is because the production of turbulent kinetic energy is large enough to dampen the unsteadiness and the URANS solution

converges with the RANS solution. The early prediction of transition is probably due to the inclusion of the pressure correction term, as we can see that the S-J correlations, which do not include this correction, can accurately predict the lift coefficient at 4^o. From 5^o upwards we can appreciate convergence between experimental, URANS, and RANS results. On the other hand, the laminar solution starts diverging from the experimental results.

An additional case where unsteady simulations are necessary is for angles of attack close to the bursting of the separation bubble, where RANS solutions tend to oscillate. We can distinguish two situations. In the former, the unsteady solver generates a steady-state solution, while in the latter, the unsteadiness persists in the form of vortex shedding on the suction side of the airfoil, as noted in Manavella (2021). It is interesting to note that if such a vortex shedding is time-averaged, as shown in Pauley et al. (1990); Manavella (2021), one obtains a closed separation bubble. That is because, in some cases, the position of the separation bubbles destabilizes the separated laminar boundary layer before the turbulence model is activated, and the vortex shedding regime generates local instantaneous reattachment of the boundary layer that switches off the production term in the turbulent kinetic energy (see Eq. (1)). For these very particular angles of attack, the simulation is close to a fully laminar situation. For low Reynolds number, this is not a problem and, as we can appreciate in Fig. 12, the laminar solutions approximate well the airfoil performance at low angles of attack. However, such behavior is not limited to low Reynolds numbers and small angles of attack, as shown in Manavella (2021). Therefore, one should be cautious in simulating within this range of angles of attack to avoid invalid results. In this work, we encountered the above-described situation only at small angles of attack, where the transition should have been close to the trailing edge. Therefore, it seems reasonable to time-average the vortex shedding solution to compute separation bubble characteristics and aerodynamic performance. Such a scenario occurs more frequently using the Suluksna-Juntasaro calibration than the Menter's calibration, as the latter is prone to activate the transition before the laminar boundary layer becomes unstable.

The analysis shows that the unsteady solver is very advantageous. It significantly improves the performance predictions for airfoils operating at low angles of attack when the flow remains laminar and in situations close to the bursting of the separation bubble. Once the transient behavior terminates, steady and unsteady solvers solutions converge, and the expensive unsteady simulations are no more convenient.

6 Application: Low Reynolds Number Airfoils: Eppler 387, Ishii and Selig/Donovan 7003.

We tested the previously developed model with different airfoils and Reynolds numbers over a wide range of angles of attack to check its applicability. We chose three popular low Reynolds number airfoils, which have been extensively tested and are known to have separation bubbles on their suction side. We carried out unsteady simulations at low angles of attack and switched to steady simulations once the unsteady solver provided steady-state solutions. In Figs. 13–17 the computed values of the aerodynamic coefficients are the time-averaged values for the unsteady simulations and the values provided by the steady solver for higher angles of attack, except when specified otherwise.

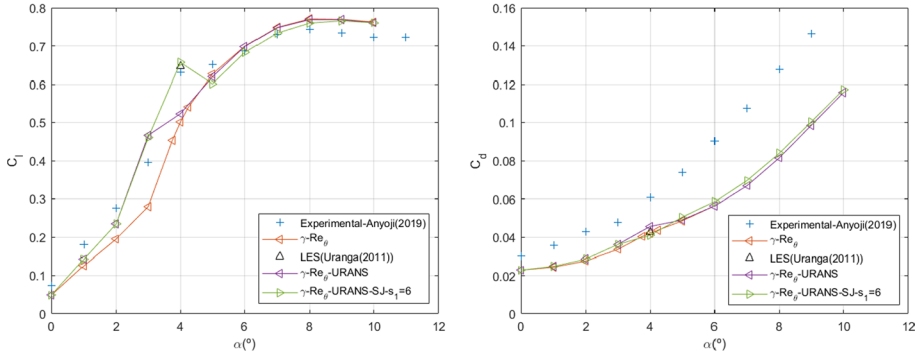

(a) Lift coefficient. **(b)** Drag coefficient.

Fig. 13 Lift and drag coefficients of airfoil SD7003 at Re=23,000

6.1 Selig/Donovan 7003 (SD7003) airfoil

For this airfoil, in addition to the Re = 60,000 results that we used for tuning, we tested two more Reynolds number conditions, Re = 23,000 and Re = 200,000. They represent two extreme conditions for the so-called very-low Reynolds number regime, and, in both cases, they present a separation bubble as shown by several authors (UIUC (2020); Anyoji and Hamada (2019)).

Considering a Reynolds number of 23,000, Fig. 13 shows a steady solver solution and two unsteady solutions, one obtained using Menter's calibration, and the other using Suluksna-Juntasaro's calibration with s_1 set to 6. As we noted in the previous section, the absence of the pressure gradient correction slightly delays the transition and results in a bit larger separation bubbles. Both unsteady polars show a significant increase in the lift for angles of attack ranging between 0 and 4°. At this Reynolds number and for small angles of attack, the flow is laminar along most of the airfoil, and the solution captures the vortex shedding regime typically seen for slightly lower Reynolds numbers when the transition is incomplete. The vortex shedding affecting part of the suction side of the airfoil generates relatively low-pressure regions, which produce a lift enhancement, as noted in Carreño Ruiz etal. (2022) in the ultra-low Reynolds number regime. Once the transition begins, the turbulence model is activated, the unsteadiness fades, and a steady flow pattern is predicted even with the unsteady solver. The Suluksna-Juntasaro's calibration offers an excellent agreement with LES data for an angle of attack of 4°for both lift and drag coefficients. Considering the non-linearity of the lift curve at such low Reynolds numbers, the agreement of the lift coefficient with results presented in Anyoji and Hamada (2019) is satisfactory. However, the drag coefficient are too high compared with the results presented by Uranga (2010) and also to our predictions.

Figure 14 shows the lift coefficient and the drag coefficient for Re = 60,000 including additional experimental results not presented in the previous section. The experimental results in Anyoji and Hamada (2019) display lift and drag coefficients that seem too high. Such a trend might be related to a misalignment of the airfoil relative to the flow. In any case, we can observe that both the results in Anyoji and Hamada (2019) and ours predict a premature stall compared to the results presented by Ol et al. (2005); Galbraith

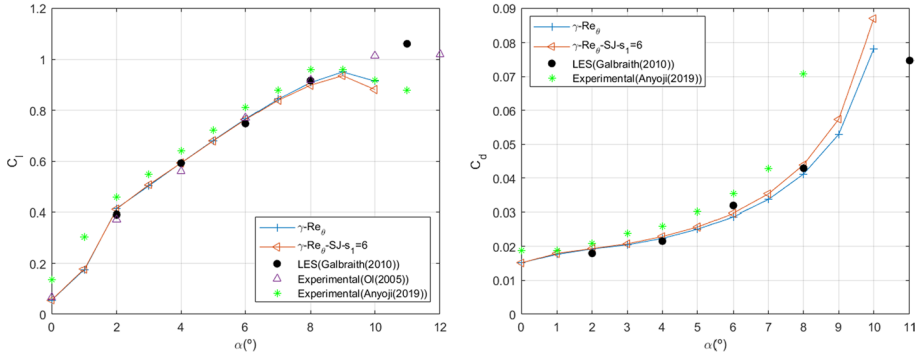

(a) Lift coefficient. **(b)** Drag coefficient.

Fig. 14 Lift and drag coefficients of airfoil SD7003 at Re=60,000

and Visbal (2010). Before stall, the agreement between the drag and lift coefficients reported by Ol et al. (2005); Galbraith and Visbal (2010) and ourselves is satisfactory.

Figure 15 illustrates the results for a considerably larger Reynolds number, 200,000. In this case, the agreement is excellent with experimental results from Selig UIUC (2020) both in lift and drag, and both calibrations produce almost identical predictions. Figure 16 shows the flow characteristics on the suction side compared to those obtained experimentally by Selig UIUC (2020) using an oil visualization technique. The size of the separation bubble is, for the considered angles of attack, consistent with the experiments by Selig UIUC (2020) where we can observe a trailing edge bubble that moves upstream as the angle of attack increases.

Finally, we compare the airfoil aerodynamic coefficients for the three tested Reynolds numbers. Figure 17 shows that the developed numerical model can capture the non-linear very-low Reynolds number effects. At Re=200,000, the lift coefficient is almost linear and matches very well with the potential airfoil theory because the separation bubble has a reduced height and is stationary for the considered range of angles of attack. On the other hand, at Re=23,000, the $c_L(\alpha)$ curve has a characteristic s-shape due to the

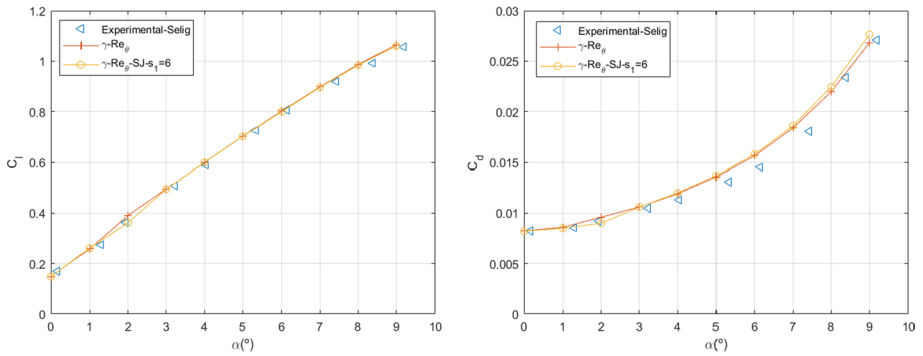

(a) Lift coefficient. **(b)** Drag coefficient.

Fig. 15 Lift and drag coefficients of airfoil SD7003 at Re=200,000 compared with experimental data from Selig UIUC (2020)

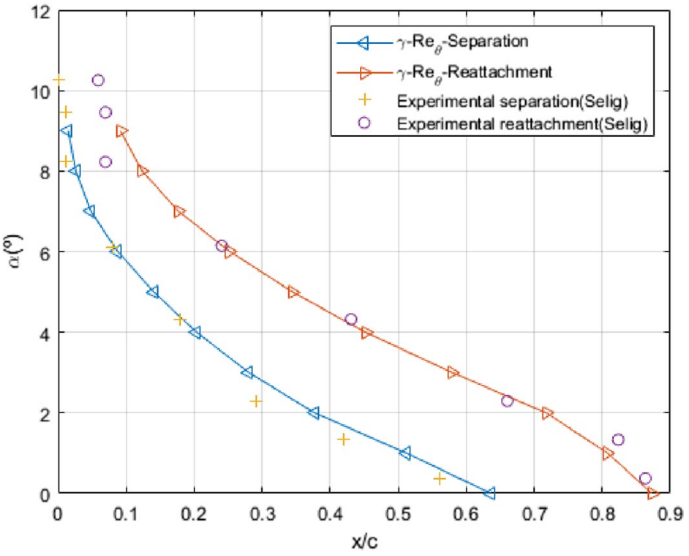

Fig. 16 Comparisons between computational and experimental location of upper surface flow features for the SD7003 airfoil at Re=200,000

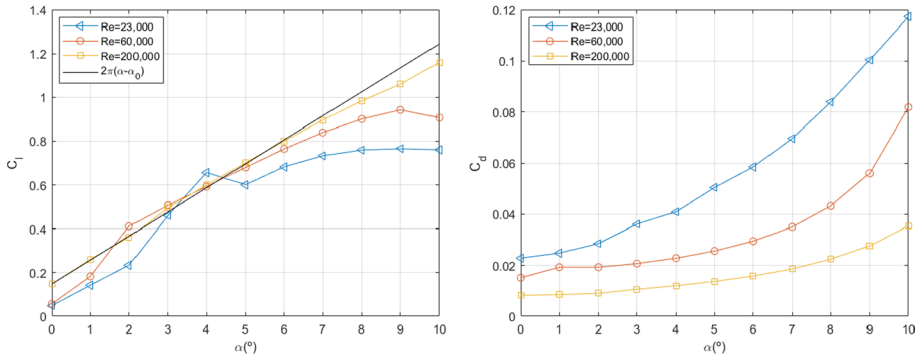

(a) Lift coefficient. **(b)** Drag coefficient.

Fig. 17 Lift and drag coefficients of airfoil SD7003 for several Reynolds numbers computed with the Suluksna-Juntasaro calibration with the s_1 parameter set to 6

increase in the lift when the boundary layer reattaches and closes the separation bubble. It is interesting to note that near the angle of attack that corresponds to the first reattachment, the curves at low Re have a lift coefficient higher than those at high Reynolds numbers, as confirmed in Uranga (2010) also. An intuitive explanation for such a behavior is that, at a low Reynolds number, the mean separation bubble is thicker, and therefore, for a short range of angles of attack, the effective camber of the airfoil is increased. The effect of increased effective camber due to the thickness of the separation bubble has been studied by Hansen et al. (2014) for slightly higher Reynolds numbers. The drag coefficient also presents some non-linearities, but the effect of the Reynolds number is

much more evident as the curves shift upwards and the curvature of their typical parabolic shape increases as the Reynolds number decreases.

6.2 Ishii Airfoil

The lift coefficients obtained by our simulations are systematically higher than the experimental data and the LES data by Anyoji et al. (2014). We suspect that there might be a mismatch between the definition of the zero angle of attack in Anyoji et al. (2014) and the present study, as the Ishii airfoil has a thick trailing edge, which could generate uncertainty on the definition of the chord line. The overprediction with respect to the LES data at small angles of attack, when the flow is still laminar, as shown by our CFD simulations and also visible in the smoke visualization by Anyoji and Hamada (2019), reinforces the idea that a geometrical mismatch is responsible for the discrepancies. To offer a reasonable comparison, Fig. 18 shows our simulation results shifted by an angle of $+0.587^o$ so that our numerical results fall on the line joining the LES data between 0 and 1°. One can see that for the smallest angles of attack, where the flow should remain laminar, both lift and drag coefficients are in good agreement with LES data. The discrepancies at and above 6° could be attributable to the 3D nature of the flow at high angles of attack, which two-dimensional simulations cannot resolve. The experimental drag coefficient presented in Anyoji et al. (2014) shows a noticeable difference with LES results and our shifted numerical results. In Anyoji et al. (2014), the authors recognized the discrepancy and reported that its cause was yet to be determined.

6.3 Eppler 387 (e-387) Airfoil

The aerodynamic characteristics of the e-387 airfoil that we show in Fig. 19 reveal a broad variability in the data obtained by different methods. For clarity, we present only one set of experimental data, but we remind that distinct facilities, and even runs in the same facility, produced inconsistent results, as reported in McGhee et al. (1988). In general, some 3D instabilities may be responsible for the boundary layer separation without reattachment at angles of attack between 3^o and 8^o, thus affecting the mean value of the flow. It is worth

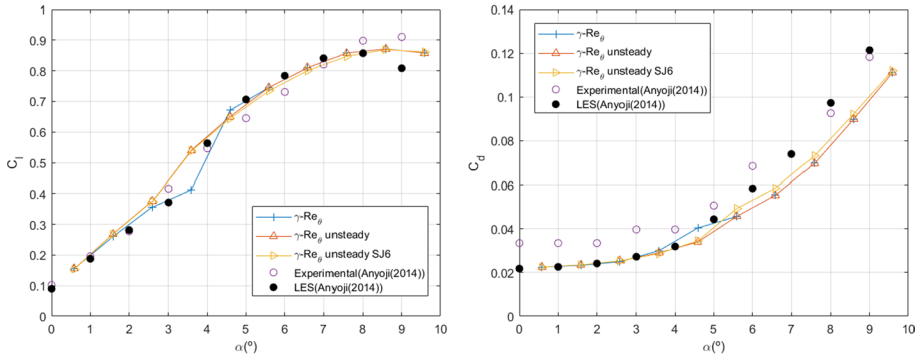

(a) Lift coefficient. **(b)** Drag coefficient.

Fig. 18 Lift and drag coefficients of the Ishii airfoil at Re=23,000. Our results have been shifted by $+0.587^o$

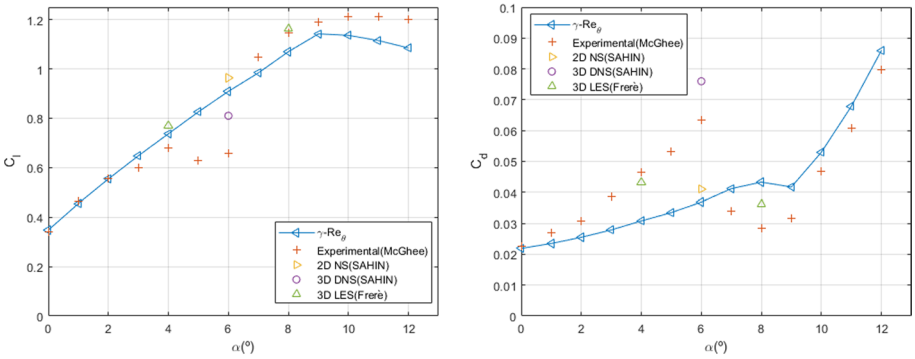

(a) Lift coefficient. **(b)** Drag coefficient.

Fig. 19 Lift and drag coefficients of the Eppler 387 airfoil at Re=60,000

mentioning that this separated regime is not found in all facilities and seems to be very sensitive to freestream turbulence levels, (McGhee et al. (1988)). The simulations presented in this paper are 2D and therefore cannot capture such instabilities, but there is a good agreement between our results and the 2D Navier-Stokes simulations performed by Sahin et al. (2008). This latter reports remarkable discrepancies between the 2D Navier-Stokes and the 3D DNS results obtained on the e-387 airfoil at Re=60,000. The reason for such a drastically different behavior between the two previously considered airfoils and the e-387 is probably related to the higher camber of the latter.

7 Conclusions

The numerical results presented in this paper show that the γ-Re $_\theta$ transition model can reproduce the 2D behavior of transition in airfoils with an accuracy that increases with the Reynolds number. For the airfoils and conditions that we tested, Menter's calibration provides a better prediction than the original Suluksna-Juntasaro calibration, despite a questionable double accounting of the effect of pressure gradients due to the inclusion of a pressure gradient correction in the former. A representative example of the low-Reynolds transition regime (Re=30,000) revealed a lack of turbulent kinetic energy production for both calibrations resulting in a failure to reattach the boundary layer after the transition, as observed in LES simulations. The problem alleviates as the Reynolds number increases. We tested two different formulations of the separation-induced transition (Eqs. (5) and (6)) and we conclude that the original formulation (Eq. (6)) performs better due to a higher limitation in the effective intermittency. We have seen that a constant value of the parameter s_1 does not allow the fine-tuning of the model to reliable existing data over a wide range of angles of attack. In the Suluksna-Juntasaro calibration, to minimize the error with respect to the available LES data, we increased the separation-induced transition parameter s_1 to a value of 6. The model replicates well the performance predictions made using Menter's calibration, showing that the pressure gradient correction has a similar effect to the separation-induced correction since both are related to the production of turbulent kinetic energy in the separated regions. Despite the similarity of the performance coefficients, in the case of Menter's calibration, the transition occurs at a slightly more upstream position than in

S-J because the pressure correction lowers the trigger value of the momentum thickness required to begin producing turbulent kinetic energy. The Suluksna-Juntasaro calibration with the adjusted constant s_1 to a value of 6 predicts the transition location closer to the LES results if compared to Menter's correlations, maintaining the accuracy in the airfoil performance coefficients obtained with the latter. Therefore, introducing another parameter in the separation-induced transition correction would be functional to simultaneously control the bubble length and position without re-tuning all the model correlations. Comparing the Suluksna-Juntasaro calibration with Menter's without including the pressure gradient correction, one can observe remarkably similar results. The justification for such an apparent insensitivity to the correlations is that the separation-induced transition terms provide considerable turbulent kinetic energy production rates in separated regions, overriding the usual production mechanisms that the model uses to reproduce natural or bypass transition.

The use of a URANS model for low and intermediate angles of attack produced significant vortex shedding that raises the lift coefficient of the airfoil, bringing it in line with high-fidelity numerical data and available experimental results. The vortex shedding regime dampens as the turbulence model becomes active in a sufficiently large part of the airfoil, eventually forming a steady bubble. Studying the influence of different calibrations on the vortex shedding regime, we noticed that the early transition found for the Menter calibration dampens vortex shedding at a lower angle of attack than the finely tuned SJ calibration. That may lead to underestimating the lift coefficient at low and intermediate angles of attack.

There is a satisfactory agreement between the computed numerical solutions and available high-fidelity numerical simulations and experimental data for Reynolds numbers ranging from 23,000 to 200,000 for the popular low-Reynolds number airfoils SD7003 and Ishii. The transition model can accurately predict the expected nonlinearity of the $c_L(\alpha)$ curve at very-low Reynolds numbers caused by flow separation and reattachment for low and intermediate angles of attack. For high angles of attack, simulations predict premature stall. On the other hand, the main limitation of the 2D simulations is evident when computing the polar of the e-387 airfoil, which has a much larger camber than the previous two airfoils. High-fidelity simulations show that the flow around this airfoil has a three-dimensional structure that significantly affects the pressure distribution on the body surface, a feature that our simulations cannot reproduce.

Funding Open access funding provided by Politecnico di Torino within the CRUI-CARE Agreement. No funds, grants, or other support was received.

Declarations

Conflict of interests The authors declare that they have no conflict of interests.

References

Abu-Ghannam, B.J., Shaw, R.: Natural transition of boundary layers-the effects of turbulence, pressure gradient, and flow history. J. Mech. Eng. Sci. **22**(5), 213–228 (1980). https://doi.org/10.1243/JMES_JOUR_1980_022_043_02

Anyoji, M., Hamada, D.: High-performance airfoil with low Reynolds-number dependence on aerodynamic characteristics. Fluid Mech. Res. Int. J. **3**(2), 76–80 (2019)

Anyoji, M., Nonomura, T., Aono, H., Oyama, A., Fujii, K., Nagai, H., Asai, K.: Computational and experimental analysis of a high-performance airfoil under low-Reynolds-number flow condition. J. Aircr. **51**(6), 1864–1872 (2014). https://doi.org/10.2514/1.C032553

Aono, H., Anyoji, M., Hamada, D., Wakui, S., Tatsukawa, T.: A study on development of airfoil shape toward low reynolds-number dependence of aerodynamic characteristics under low-Reynolds-number-flow conditions. In: 2018 AIAA Aerospace Sciences Meeting. https://doi.org/10.2514/6.2018-1085

Babajee, J.: Detailed numerical characterization of the separation-induced transition, including bursting, in a low-pressure turbine environment. PhD thesis, École Centrale de Lyon (2013)

Burgmann, S., Dannemann, J., Schröder, W.: Time-resolved and volumetric piv measurements of a transitional separation bubble on an sd7003 airfoil. Exp. Fluids **44**(4), 609–622 (2008)

Carreño Ruiz, M., D'Ambrosio, D.: Aerodynamic optimization of quadrotor blades operating in the martian atmosphere. In: AIAA SCITECH 2022 Forum. https://doi.org/10.2514/6.2022-0743. AIAA-2022-0743

Carton de Wiart, C., Hillewaert, K.: DNS and ILES of transitional flows around a SD7003 using a high order discontinuous Galerkin method. In: 7th International Conference on Computational Fluid Dynamics (ICCFD7) (2012)

Catalano, P., Tognaccini, R.: RANS analysis of the low-Reynolds number flow around the SD7003 airfoil. Aerosp. Sci. Technol. **15**(8), 615–626 (2011). https://doi.org/10.1016/j.ast.2010.12.006

Choudhry, A., Arjomandi, M., Kelso, R.: A study of long separation bubble on thick airfoils and its consequent effects. Int. J. Heat Fluid Flow **52**, 84–96 (2015). https://doi.org/10.1016/j.ijheatfluidflow.2014.12.001

Corral, R., Gisbert, F.: Prediction of separation-induced transition using a correlation-based transition model. Turbo Expo: Power for Land, Sea, and Air, vol. Volume 7: Turbomachinery, Parts A, B, and C, pp. 897–908 (2010). https://doi.org/10.1115/GT2010-23239

Dini, P., Maughmer, M.D.: A computationally efficient modelling of laminar separation bubbles. NASA-CR-185854 (1989)

Drela, M.: Low-Reynolds-number airfoil design for the M.I.T Daedalus prototype- A case study. J. Aircraft. **25**(8), 724–732 (1988). https://doi.org/10.2514/3.45650

Drela, M.: XFOIL: An analysis and design system for low Reynolds number airfoils. In: Low Reynolds Number Aerodynamics. Lecture Notes in Engineering, vol. 54. Springer (1989)

Eppler, R., Somers, D.M.: A computer program for the design and analysis of low-speed airfoils. NASA-TM-80210 (1980)

Frère, A., Sörensen, N.N., Hillewaert, K., Winckelmans, G.: Discontinuous Galerkin methodology for large-eddy simulations of wind turbine airfoils. J. Phys: Conf Series **753**, 022037 (2016). https://doi.org/10.1088/1742-6596/753/2/022037

Galbraith, M.C., Visbal, M.R.: Implicit large eddy simulation of low-Reynolds-number transitional flow past the SD7003 airfoil. In: 40th AIAA Fluid Dynamics Conference and Exhibit (2010). AIAA 2010-4737

Gaster, M.: The structure and behaviour of laminar separation bubbles. Aeronautical Research Council Reports and Memoranda No. 3595 (1967)

Götten, F., Finger, D.F., Havermann, M., Marino, M., Bil, C.: A highly automated method for simulating airfoil characteristics at low Reynolds number using a RANS-transition approach. In: German Aerospace Congress 2019 (2019)

Hain, R., Kähler, C.J., Radespiel, R.: Dynamics of laminar separation bubbles at Low-Reynolds-number aerofoils. J. Fluid Mech. **630**, 129–153 (2009)

Hansen, K., Kelso, R., Choudhry, A., Arjomandi, M.: Laminar separation bubble effect on the lift curve slope of an airfoil. In: 19th Australasian Fluid Mechanics Conference, RMIT University, pp. 8–11 (2014)

Langtry, R.B.: A correlation-based transition model using local variables for unstructured parallelized CFD codes. Universität Stuttgart, Fakultät Maschinenbau (2006)

Langtry, R.B., Menter, F.R.: Correlation-based transition modeling for unstructured parallelized computational fluid dynamics codes. AIAA J. **47**(12), 2894–2906 (2009). https://doi.org/10.2514/1.42362

Langtry, R.B., Menter, F., Likki, S., Suzen, Y., Huang, P., Völker, S.: A correlation-based transition model using local variables - Part II: Test cases and industrial applications. J. Turbomach. **128**(3), 423–434 (2006). https://doi.org/10.1115/1.2184353

Malan, P., Suluksna, K., Juntasaro, E.: Calibrating the $\gamma - Re_\theta$ Transition model for commercial CFD. In: 47^{th} AIAA Aerospace Sciences Meeting Including The New Horizons Forum and Aerospace Exposition (2009). AIAA-2009-1142

Manavella, A.: Low Reynolds number propeller performance validation by CFD analysis and reduced order models. Master's thesis, Politecnico di Torino (2021). https://webthesis.biblio.polito.it/18279/

McGhee, R.J., Walker, B.S., Millard, B.F.: Experimental results for the Eppler 387 airfoil at low reynolds numbers in the Langley Low-Turbulence pressure tunnel. NASA-TM-4062, NASA Langley Research Center (1988)

Menter, F.R.: Two-equation Eddy-Viscosity turbulence models for engineering applications. AIAA J. **32**(8), 1598–1605 (1994). https://doi.org/10.2514/3.12149

Menter, F.R., Langtry, R., Völker, S.: Transition modelling for general purpose CFD codes. Flow Turbul. Combust. **77**, 277–303 (2006). https://doi.org/10.1007/s10494-006-9047

Menter, F.R., Smirnov, P.E., Liu, T., Avancha, R.: A one-equation local correlation-based transition model. Flow Turbul. Combust. **95**, 583–619 (2015). https://doi.org/10.1007/s10494-015-9622-4

Menter, F.R., Langtry, R., Likki, S., Suzen, Y., Huang, P., Völker, S.: A correlation-based transition model using local variables: Part i-model formulation. In: Turbo Expo: Power for Land, Sea, and Air, vol. 41693, pp. 57–67 (2004)

Ol, M.V., McCauliffe, B., Hanff, E., Scholz, U., Kähler, C.: Comparison of laminar separation bubble measurements on a Low Reynolds number airfoil in three facilities. In: 35th AIAA Fluid Dynamics Conference and Exhibit, AIAA-2005-5149 (2005)

Park, D., Shim, H., Lee, Y.: Piv measurement of separation bubble on an airfoil at low Reynolds numbers. J. Aerosp. Eng. **33**(1), 04019105 (2020)

Pauley, L.L., Moin, P., Reynolds, W.C.: The structure of two-dimensional separation. J. Fluid Mech. **220**, 397–411 (1990)

Peric, M., Ferguson, S.: The advantage of polyhedral meshes. Dynamics **24**, 45 (2005)

Radespiel, R., Windte, J.: Numerical simulation of laminar separation bubbles with RANS solutions. In: Low Reynolds Number Aerodynamics on Aircraft Including Applications in Emerging UAV Technology, RTO-EN-AVT-104 (2003). https://doi.org/10.14339/RTO-EN-AVT-104

Rumsey, C.L., Spalart, P.R.: Turbulence model behavior in low Reynolds number regions of aerodynamic flowfields. AIAA J. **47**(4), 982–993 (2009). https://doi.org/10.2514/1.39947

Rumsey, C.: Langley research center. turbulence modeling resource. 2D NACA 0012 airfoil validation case. Effect of Farfield Boundary. https://turbmodels.larc.nasa.gov/naca0012_val_ffeffect.html. Accessed: January 24, 2022 (2014)

Sahin, M., Hall, J., Mohseni, K.: Direct numerical simulation of separated Low-Reynolds number flows around an Eppler 387 Airfoil. In: 46th AIAA Aerospace Sciences Meeting and Exhibit (2008). https://doi.org/10.2514/6.2008-422. AIAA-2008-422

Salimipour, E.: A modification of the k-kl-ω turbulence model for simulation of short and long separation bubbles. Comput. Fluids **181**, 67–76 (2019)

Schlichting, H., Gersten, K.: Boundary-layer Theory. Springer, USA (2016)

Selig, M.: Low Reynolds number airfoil design lecture notes. VKI Lecture Series, November, 24–28 (2003)

Siemens Digital Industries Software: Simcenter STAR-CCM+ User Guide V. 2019.3

Spalart, P.R., Rumsey, C.L.: Effective inflow conditions for turbulence models in aerodynamic calculations. AIAA J. **45**(10), 2544–2553 (2007)

Suluksna, K., Dechaumphai, P., Juntasaro, E.: Correlations for modeling transitional boundary layers under influences of freestream turbulence and pressure gradient. Int. J. Heat Fluid Flow **30**(1), 66–75 (2009)

UIUC Applied Aerodynamics Group: Low Reynolds number airfoil data and documentation. https://m-selig.ae.illinois.edu/uiuc_lsat.html. Accessed: March 13, 2020

Uranga, A.: Investigation of transition to turbulence at low Reynolds numbers using Implicit Large Eddy Simulations with a discontinuous galerkin method. University of California, Berkeley (2010)

Uranga, A., Persson, P.-O., Drela, M., Peraire, J.: Implicit large eddy simulation of transitional flows over airfoils and wings. In: 19th AIAA Computational Fluid Dynamics (2009). AIAA 2009-4131

Walters, D.K., Cokljat, D.: A three-equation eddy-viscosity model for Reynolds-Averaged Navier-Stokes simulations of transitional flow. ASME J Fluids Eng (2008). https://doi.org/10.1115/1.2979230